1
Nanostructured Activated Carbons for Supercapacitors

Wentian Gu, Xinran Wang, and Gleb Yushin

1.1
Supercapacitors

Production and storage of clean and renewable energy has become one of the most exciting yet challenging topics in recent decades. The pressing need for green energy production and efficient energy storage has been further emphasized by the shortage of conventional energy sources and the continuous environment deterioration. While many forms of natural energy, such as solar, wind, and water power, have been considered candidates for the next-generation energy sources, electrochemical energy storage devices, such as rechargeable batteries and supercapacitors, dominate the solutions for the transmittance and storage of renewable energy. By now, these devices have been commercialized and applied in a wide range of industries, ranging from portable electronics to transportation to military and aerospace.

A significant performance gap exists between the energy and power performance characteristics of batteries and electrolytic capacitors, as shown in Figure 1.1. Batteries offer very high specific energy and energy density (energy stored per unit mass or volume of a device), but suffer from relatively low specific power and power density. Conversely, electrolytic capacitors offer excellent power density characteristic at the expense of lower energy density. Electrochemical capacitors (which are often called supercapacitors) nearly bridge the existing gap in performance, by offering moderate energy and power characteristics. In contrast to batteries, supercapacitors additionally offer significantly longer cycle stability and broader temperature window of efficient applications.

On the basis of the differences in energy storage mechanisms, supercapacitors can be classified into two broad categories. One is the electrical double-layer capacitor (EDLC), in which the capacitance comes from the pure electrostatic charge accumulated across the so-called double layer at the electrode/electrolyte interface. The large surface area of the EDLC electrodes combined with a small thickness of the double layer results in a specific and volumetric capacitance two orders of magnitude larger than that of the electrolytic capacitors (Figure 1.1). The second category is a pseudocapacitor, in which fast and reversible Faradic

Nanocarbons for Advanced Energy Storage, Volume 1, First Edition. Edited by Xinliang Feng.

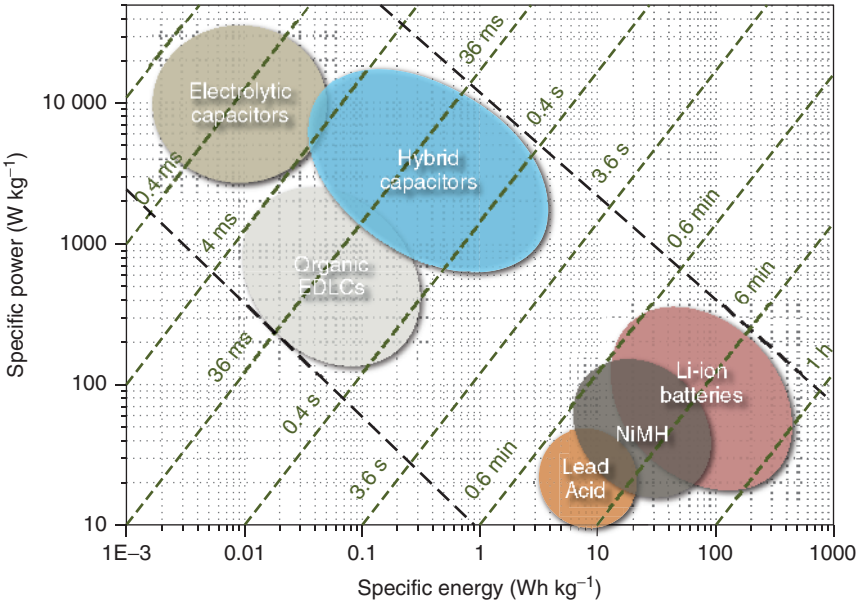

Figure 1.1 Schematic illustration of the specific power versus specific energy for various electrical energy storage devices.

(charge transfer) processes take place across the electrode/electrolyte interface. Quite often, these two mechanisms may function simultaneously in many supercapacitors.

The energy density of supercapacitors is dependent on the capacitance of their electrodes and the maximum operating voltage. The latter is determined by the window of electrochemical stability of the electrolyte. Such stability windows, however, may be influenced by the surface chemistry and other properties of the supercapacitor electrodes as well as electrolyte purity.

The energy of an EDLC could be estimated according to following equation:

$$E^{\mathrm{EDLC}} = \left(\frac{C_- \cdot C_+}{C_- + C_+}\right) \cdot \left(V_{\max}^{\mathrm{EDLC}}\right)^2 \tag{1.1}$$

where E is the energy, $V_{\max}$ is the maximum voltage difference between two electrodes, C_+ and C_- are the capacitances of the positive and negative electrodes, respectively. The energy of an EDLC is maximized when C_+ and C_- are identical:

$$E^{\mathrm{EDLC}} = \frac{1}{2} C \cdot \left(V_{\max}^{\mathrm{EDLC}}\right)^2 \tag{1.2}$$

In a symmetric EDLC, the specific capacitance of each electrode (capacitance per unit mass of the electrode material) could be identified by a galvanostatic (constant current) charge–discharge test, where the specific capacitance is calculated using the following equation:

$$C = I\, \mathrm{d}t/\mathrm{d}V \tag{1.3}$$

where C is the specific (normalized by an electrode mass) capacitance, I is the specific current, and dv/dt is the changing rate of the voltage. In an ideal EDLC, the voltage slope, dv/dt, is constant for a fixed current.

The calculation of a pseudocapacitance (or a total capacitance, which includes both pseudocapacitors and a double-layer capacitance) could be similar to that of a pure double-layer capacitance, in case when dv/dt stays constant, in spite of the additional Faradic reactions. If dv/dt varies with time, one may approximate the capacitance by using an average value of the voltage slope. We shall note that because of lower cost, faster rate, longer cycle life, and lower self-discharge, EDLC-type of supercapacitors currently dominate the market. The current market fraction for pseudocapacitors is tiny.

1.2
Activated Carbon as Electrode for Supercapacitors

In addition to high capacitance, other desirable properties of electrode materials for EDLCs include (i) Free of uncontrolled side reactions with utilized electrolyte to achieve a low self-discharge and long cycle life; (ii) low cost; (iii) abundance; (iv) low toxicity and health hazard; (v) scalability of the synthesis; (vi) mechanical, chemical, and electrochemical stability during the device assembling and operation; (vii) high packing density; and (viii) reliable and reproducible properties.

By now, high-surface-area carbon materials are utilized in EDLCs, with activated carbons (ACs) taking nearly all of the current market. The large specific surface area (SSA) of ACs, their relatively high chemical stability, somewhat reasonable cost, abundance, and diversity of AC precursors, biocompatibility, scalable synthesis, and other useful properties make ACs the choice of the device manufacturers. ACs could be produced in various shapes and forms, such as powders and fibers of various size and pore size distributions, mats, monoliths, films, foils.

Many raw materials, natural and artificial, have been utilized as precursors for AC synthesis. The pore size of ACs can be partially controllable by selecting particular precursor chemistry, activation method, and conditions. Still, commercial ACs for use in EDLCs suffer from some limitations, such as the presence of bottle neck pores, high resistance to ion diffusion and limited volumetric and gravimetric capacitance, to name a few. With the goal of efficient ion diffusion and reduction in equivalent series resistance (ESR), several routes for a more delicate control on the pore size distribution and microstructure of ACs have recently been explored.

In this chapter, we review the development of nanostructured ACs as electrode materials for EDLCs. In Sections 1.3 and 1.4, we review the precursors and processes for AC synthesis in various shapes and forms. In Section 1.5, we review the key factors determining the performance of AC-based EDLCs, including the porous texture of the electrode, the electrical and ionic conductivity within the

electrode, and the electrolyte selection. In Section 1.6, we discuss some of the AC properties, which may induce self-discharge within EDLCs.

1.3 Synthesis of ACs

1.3.1 Precursors

ACs are prepared by thermal treatment and partial oxidation of organic compounds, including a very wide selection of natural and synthetic precursors. Most of the pores in ACs are in the 0.4–4 nm range, and the pore size distribution is generally relatively broad. Some of the most common natural precursors for AC synthesis include nutshells (mostly coconut shells [1–8]), waste wood products, coal, petroleum coke, pitch, peat, lignite, while other precursors, such as starch, sucrose, corn grain, leaves, seaweed, alginate, straw, coffee grounds are also occasionally used (Tables 1.1–1.3) [9–28]. More advanced (and unfortunately more expensive) ACs with reproducible properties, more uniform microstructure

Table 1.1 Physical properties of the ACs from various precursors.

Precursors		Density of carbon (g cm^{-3})	Carbon yield (wt%)	Conductivity	References
Natural precursor	Coconut shell	1.834–2.131	25–40	—	[1, 2, 4–8, 36, 37]
	Pitch	0.54–0.75	33.6	22 Ω	[16, 17, 38–41]
	Starch	—	—	0.1 Ω	[13, 42, 43]
	Seaweed	0.47–0.80	16	–	[44, 45]
	Coal	—	40	—	[16, 19]
	Apricot shell	0.504	23.2	—	[20]
	Ramie	—	38.1	0.08 Ω	[46]
	Sugarcane bagasse	—	34.2	—	[18]
	Wheat straw	—	37	0.62–1.63 Ω	[22]
	Petroleum residue (ethylene-tar)	—	—	0.6 Ω	[47]
	Egg shell	—	—	0.018 Ω m	[28]
Artificial precursor	Polyacrylonitrile	—	30	4.91 ($S \cdot cm^{-1}$)/0.5 Ω	[48]
	Poly(vinylidene chloride)	—	18–22	0.1 Ω	[49–51]
	Poly(amide imide)	—	55	—	[52]
	Phenol formaldehyde resin	—	40	—	[53]
	Polybenzimidazole	1.2	49	9 $S \cdot cm^{-1}$	[54]
	Sulfonated poly(divinylbenzene)	0.66	—	—	[33]
	Polystyrene	—	48	—	[55]

Table 1.2 Activated method on the pore characterization of different ACs precursors.

Precursors		Activation method	Activation agent	S_{BET} ($m^2\ g^{-1}$)	Pore volume ($cm^3\ g^{-1}$)	Average pore size (nm)	Pore size distribution ($cm^3 \cdot g^{-1}$)		References
							V_{micro}	V_{meso}	
Natural precursor	Coconut shell	Physical	CO_2	750–1360	0.255–0.521	0.78–1.47	0.2–0.5	0.6–1	[1]
		Physical	CO_2	2000	0.5319	—	0.3482	0.1837	[3]
		Thermal	—	183	—	—	0.5–0.6	—	[2]
		Chemical	Urea	898	0.483	1.57	0.454	0.029	[36]
		Chemical	KOH	2451	1.21	1.98–2.09	1.04	0.17	[4]
		Chemical	$ZnCl_2$	1091–2114	0.681–1.307	1.15–1.25	0.549–1.142	—	[6]
		Chemical	K_2CO_3	—	1.5	—	0.7	0.8	[7]
	Pitch	Chemical	KOH	2750	1.227	1.82	1.048	0.198	[16]
		Chemical	KOH	2583	2.35	1.29	0.16	1.13	[17]
		Chemical	KOH	770	0.42	1.468	—	—	[38]
		Chemical	KOH	1848.3	0.98	1.41	—	—	[38]
		Chemical	KOH	1965	—	2	—	—	[39]
		Chemical	KOH	3204	1.57	1.7	1.02	0.55	[40]
		Chemical	KOH	3160	1.58	—	—	—	[41]
	Coal	Chemical	KOH	2860	1.63	2.3	1.35	0.28	[16]
		Chemical	KOH	3506	1.51	—	0.68	0.63	[19]
	Seaweed	Physical	CO_2	3487	—	—	—	—	[44]
		—	—	1650	—	—	81.1%	18.9%	[45]

(continued overleaf)

Table 1.2 (*Continued*)

Precursors		Activation method	Activation agent	S_{BET} ($m^2\ g^{-1}$)	Pore volume ($cm^3\ g^{-1}$)	Average pore size (nm)	Pore size distribution ($cm^3 \cdot g^{-1}$)		References
							V_{micro}	V_{meso}	
Natural precursor	Starch	Chemical	KOH	1510	—	—	18.4%	81.6%	[13]
	Apricot shell	Chemical	NaOH	2335	0.984	—	0.8	0.184	[20]
	Viscose fibers	Chemical	KOH	1978	1.85	—	0.93	0.92	[56]
	Petroleum residue (ethylene–tar)	Chemical	KOH	2652	1.27	1.12	0.79	0.33	[47]
	Ramie	Chemical	$ZnCl_2$	2087	—	2.07	—	—	[46]
	Banana fiber	Chemical	$ZnCl_2$	1907	—	0.23	—	—	[10]
	Corn grain	Physical	CO_2	3420	1.895	1.03	1.37	0.858	[15]
	Coffee ground	Chemical	$ZnCl_2$	1019	0.48	—	0.21	0.27	[21]
	Celtuce leaves	Chemical	KOH	3404	1.88	2.2	—	—	[23]
	Seed shells	Chemical	KOH	2132	2.18	1.4	0.96	1.22	[26]
	Sugarcane bagasse	Chemical	$ZnCl_2$	1788	1.74	1.5	0.191	1.55	[18]
	Wheat straw	Chemical	KOH	2316	1.496	—	—	—	[22]
	Beer lees	Chemical	KOH	3557	2.138	1.176	—	—	[24]
	Camellia oleifera shell	Chemical	$ZnCl_2$	2080	1.18	2.3	0.12	1.06	[25]
	Argan seed shell	Chemical	KOH/melamine	2062	3.03	1.4	1.99	1.04	[26]
	Sucrose	Physical	CO_2	3000	1.26	—	1.03	0.23	[11]
		Physical	CO_2	1941	0.91	—	0.87	0.04	[12]
	Rice husk	Chemical	H_2SO_4	—	—	—	—	—	[27]
	Wood dust	Chemical	KOH	2967	1.35	—	1.2	0.15	[14]
		Chemical	KOH	913	0.61	—	0.33	0.28	[57]
	Egg shell	Chemical	KOH	1575	0.98	—	—	—	[28]

Artificial precursor	Cellulose	Chemical	KOH	2457	1.08	—	0.94	0.14	[14]
	Polyacrylonitrile	Chemical	NaOH	3291	2.162	—	0.74	1.43	[20]
	Polyaniline	Chemical	NaOH	398.7	0.617	6.19	0.049	0.568	[34]
		Chemical	K_2CO_3	917	0.133	1.39	—	—	[31]
	Poly(vinylidene chloride)	Chemical	KOH	2100	—	0.9	—	—	[49]
		Physical	CO_2	771.9	0.41	1.47	—	—	[51]
	Poly(amide imide)	Physical	CO_2	1360	1	—	0.8	0.2	[52]
	Polyvinyl alcohol	Chemical	KOH	2218	1.15	2.25	0.87	0.28	[58]
	Phenol formaldehyde resin	Chemical	KOH/$ZnCl_2$	2387	1.2	2	0.1	1.1	[53]
	Polybenzimidazole	Physical	H_2O	1220	0.91	0.64	0.71	0.2	[54]
	Sulfonated poly(divinylbenzene)	Physical	CO_2	2420	1.43	1.7	0.87	0.662	[33]
	Polypyrrole	Chemical	KOH	3432	2.39	—	0.81	1.58	[14]
	Polystyrene	Chemical	KOH	2350	1.32	2.25	0.88	0.44	[55]

Table 1.3 Capacitive performance of AC-based supercapacitors.

Precursor		Activation method	Activation agent	Reported capacitance ($F\ g^{-1}$)/cell type	Electrolyte	References
Natural precursor	Coconut shell	Chemical	Melamine and urea	230/2 symm	1 M H_2SO_4 aq. sol.	[36]
		—	—	36/2 symm	1 M $LiClO_4$ in PC	[39]
	Pitch	Physical	H_2O	28/2 symm	1 M KCl aq. sol.	[59]
		Chemical	KOH	261/2 symm	1 M H_2SO_4 aq. sol.	[16]
		Chemical	KOH	148/2 symm	1 M Et_4NBF_4/PC	[17]
		Chemical	KOH	220/2 symm	2 M H_2SO_4 aq. sol.	[40]
		Chemical	KOH	295/2 symm	2 M H_2SO_4 aq. sol.	[41]
		Chemical	KOH	46/2 symm	$TEABF_4$ in PC	[60]
		Chemical	KOH	130/2 symm	1 M H_2SO_4 aq. sol.	[61]
		—	—	24/2 symm	1 M $LiClO_4$ in PC	[39]
	Coal	Chemical	KOH	312/2 symm	1 M H_2SO_4 aq. sol.	[16]
		Chemical	KOH	220/2 symm	1.0 M $LiClO_4$/PC	[19]
	Seaweed	Physical	CO_2	264/2 symm	1 M H_2SO_4 aq. sol.	[44]
		—	—	198/3	1 M H_2SO_4 aq. sol.	[45]
	Starch	Chemical	KOH	194/2 symm	30 wt% KOH aq. sol.	[13]
	Apricot shell	Chemical	NaOH	339/2 symm	6 M KOH aq. sol.	[20]
	Viscose fibers	Chemical	KOH	340/3	4 M H_2SO_4 aq. sol.	[56]
	Petroleum residue (ethylene tar)	Chemical	KOH	334/2 symm	1 M H_2SO_4 aq. sol.	[47]
	Argan seed shell	Chemical	KOH	355/3	1 M H_2SO_4 aq. sol.	[26]
	Banana fiber	Chemical	$ZnCl_2$	74/2 symm	1 M Na_2SO_4 aq. sol.	[10]
	Corn grain	Chemical	KOH	257/2 symm	6 M KOH aq. sol.	[15]
	Celtuce leaves	Chemical	KOH	273/2 symm	2 M KOH aq. sol.	[23]
	Coffee ground	Chemical	$ZnCl_2$	368/2 symm	1 M H_2SO_4 aq. sol.	[21]

	Sugarcane bagasse	Chemical	$ZnCl_2$	300/2 symm	1 M H_2SO_4 aq. sol.	[18]
	Wheat straw	Chemical	KOH	251/2 symm	$MeEt_3NBF_4$/AN	[22]
	Beer lees	Chemical	KOH	188/3	0.1 M H_2SO_4 aq. sol.	[24]
	Camellia oleifera shell	Chemical	$ZnCl_2$	184/3	6 M KOH aq. sol.	[25]
		Chemical	$ZnCl_2$	230/3	1 M H_2SO_4 aq. sol.	[25]
	Sucrose	Physical	CO_2	160/2 symm	1 M H_2SO_4 aq. sol.	[11]
		Physical	CO_2	170/2 symm	N-Ethyl-dimethyl-propyl-ammonium bis (trifluoromethylsulfonyl)imide ($EdMPNTf_2N$)	[12]
	Glucose	Chemical	KOH	220/3	1 M Na_2SO_4 aq. sol.	[62]
	Rice husk	Chemical	H_2SO_4	175/3	6 M KOH aq. sol.	[27]
	Wood sawdust	Physical	CO_2	138/2 symm	1 M H_2SO_4 aq. sol.	[57]
		Chemical	KOH	143/2 symm	6 M KOH aq. sol.	[14]
		Chemical	KOH	236/2 symm	1 M $TEABF_4$ in AN	[14]
	Egg shell	Chemical	KOH	297/3	6 M KOH aq. sol.	[28]
Artificial precursor	Polyacrylonitrile	—	—	66/2 symm	1 M $LiPF_6$ in EC-DEC	[63]
		—	—	90/2 symm	1 M $TEABF_4$ in PC	[64]
		—	—	202/2 symm	1 M H_2SO_4 aq. sol.	[48]
		Chemical	$ZnCl_2$	174/2 symm	6 M KOH aq. sol.	[65]
		Chemical	O_2	150/2 symm	1 M H_2SO_4 aq. sol.	[66]
		Chemical	NaOH	196/2 symm	$LiN(SO_2CF_3)^2 + C_3H_5NO_2$	[20]
	Phenol resin	Chemical	2 M HNO_3	60/2 symm	6 M KOH aq. sol.	[67]
		Chemical	$KOH/ZnCl_2$	142/2 symm	1 M Et_3MeNBF_4 in PC	[53]
		Chemical	KOH	100/2 symm	1 M H_2SO_4 aq. sol.	[68]
		—	—	3/2 symm	1 M $LiClO_4$ in PC	[39]
		—	—	18/2 symm	1 M $LiClO_4$ in PC	[39]
		—	—	40/2 symm	1 M H_2SO_4 aq. sol.	[39]

(continued overleaf)

Table 1.3 (*Continued*)

Precursor		Activation method	Activation agent	Reported capacitance ($F\,g^{-1}$)/cell type	Electrolyte	References
Artificial precursor		—	—	171/3	6 M KOH aq. sol.	[69]
	Polyaniline	—		125/3	6 M KOH aq. sol.	[34]
	Poly(vinylidene chloride)	Chemical	KOH	38/2 symm	1 M $TEABF_4$ in PC	[49]
		—	—	64/2 symm	1 M H_2SO_4 aq. sol.	[51]
	Poly (amide imide)	Physical	CO_2	196/3	6 M KOH aq. sol.	[52]
	Polyvinyl alcohol	Chemical	KOH	115/2 symm	1 M Et_3MeNBF_4 in PC	[35]
		Chemical	KOH	147/2 symm	1 M $LiPF_6$ in EC-DEC	[35]
		Chemical	KOH	218/2 symm	30 wt% KOH aq. sol.	[35]
	Polybenzimidazole	Chemical	N_2	23/2 symm	0.8 M $TEABF_4$ in PC	[54]
	Sulfonated poly(divinylbenzene)	Physical	CO_2	206/3	2 M H_2SO_4 aq. sol.	[33]
	Lignocellulosic materials	—	—	95/2 symm	1.5 M $TEABF_4$ in AN	[70]
		—	—	125/2 symm	1.7 M $N(C_2H_5)_4CH_3SO_3$ in AN	[71]
	Polystyrene	Chemical	KOH	258/3	6 M KOH aq. sol.	[55]
	Polythiophene	Chemical	KOH	230/2 symm	1 M HCl aq. sol.	[72]
	Polypyrrole	Chemical	KOH	300/2 symm	$EMImBF_4$	[29]
	Graphite	Chemical	HNO_3/H_2SO_4 (1 : 1)	1071/3	0.1 M KOH aq. sol.	[73]
	Styrene-divinylbenzene	Chemical	H_3PO_4	210/2 symm	1 M H_2SO_4 aq. sol.	[74]
	Resorcinol and formaldehyde	—	—	198/2 symm	2 M H_2SO_4 aq. sol.	[75]
		—	—	199/3	6 M KOH aq. sol.	[76]
	Dimethylacetamide/ polybenzimidazole	—	—	178/2 symm	30 wt% KOH aq. sol.	[77]

and pores, and often better developed porosity (higher SSA) can be produced from synthetic polymers, such as polyacrylonitrile (PAN), polyvinylidene chloride (PVDC), polyfurfuryl alcohol (PFA), polyvinyl chloride (PVC), polypyrrole (PPy), polyaniline (PANI), polydivinylbenzene (PDVB) [9, 29–35], to mention a few. Most organic materials rich in carbon that do not fuse upon thermal decomposition can be used as precursors. Some physical properties of the selected precursors for ACs synthesis are listed the following sections:

1.3.2 Activation Method

Current methods for the preparation of ACs are often classified into two categories: physical (or thermal) activation and chemical activation. On the basis of some of the representative works, the porous structures of ACs activated from different activation methods are summarized in Table 1.2.

1.3.2.1 Physical Activation

Production of ACs by physical activation commonly involves two steps: carbonization of a precursor (removal of noncarbon species by thermal decomposition in inert atmosphere) and gasification (development of porosity by partial etching of carbon during annealing with an oxidizing agent, such as CO_2, H_2O, or a mixture of both) [78, 79]. In some cases, low-temperature oxidation in air (at temperatures of 250–350 °C) is occasionally performed on polymer precursors to increase the carbon yield. The reactions occurring during the physical activation could be simplified to the following:

$$C + H_2O \rightarrow H_2 + CO$$

$$C + 2H_2O \rightarrow 2H_2 + CO_2$$

$$C + CO_2 \rightarrow 2CO$$

It has to be pointed out that all these reactions are endothermic [80, 81]. This provides better control over the temperature uniformity and activation rate within the powder, but requires sufficient thermal energy (commonly heating to above 800 °C) and a relatively long (hours) period of activation for generating high SSA and pore volume. Such porosity development during activation commonly results in 20–30 wt% yield (oxidation of 60–80 wt% of the initial carbon to CO), which may be considered a critical drawback of physical activation.

1.3.2.2 Chemical Activation

Chemical activation is one-pot preparation method for ACs, utilizing the microexplosion behavior of the activating agent. Production of ACs by chemical activation generally involves the reaction of a precursor with a chemical reagent (such as KOH [40, 41, 49, 61, 68], H_3PO_4 [74], $ZnCl_2$ [65], H_2SO_4 [73], among a few) at elevated temperatures. Compared to physical activation, chemical

activation generally results in smaller pores, higher carbon yield, and more uniform pore size distribution [82–84].

KOH and NaOH are among the most effective chemical agents for porosity development. The pores are believed to be created via both exfoliation and partial oxidation of carbon [85]. This commonly leads to a larger volume of micropores formed (Table 1.2) and often high carbon yield. The mechanism of carbon etching during metal hydroxide activation can be qualitatively expressed as follows:

$$4MOH + C \rightarrow M_2CO_3 + M_2O + 2H_2 \quad (\text{where M} = \text{K or Na})$$

Chemical activation methods commonly result in higher specific capacitance in both aqueous and organic electrolytes [86–88]. For example, Kierzek *et al*. [16] chemically activated highly volatile coal by utilizing KOH. The produced AC exhibited SSA of 3150 $m^2 g^{-1}$ with the pore volume of 1.61 $cm^3 g^{-1}$. Its application in EDLC showed a specific capacitance of 300 F g^{-1} and 9.9 μF cm^{-2} in 1 M H_2SO_4 (aq. solution) electrolyte. This capacitance is very high and superior to the reported performance of one of the most promising commercial ACs, PX 21 (240 F g^{-1} and 8 μF cm^{-2}) when measured under the same conditions.

For some precursors, however, well-developed porosity is difficult to achieve even by using chemical activation. For example, Hwang *et al*. [89] systematically investigated variations in the activation process of sewage sludge and coal tar pitch as carbon precursors, by varying the activation temperature, operation time, and activating agent concentration. The total surface area of AC from KOH and NaOH were found to be only 450 and 381 $m^2 g^{-1}$ with the pore volume of 0.394 and 0.37 $cm^3 g^{-1}$, respectively. The more open porous texture from KOH activation is attributed to the larger ionic radius of K^+, which is 0.27 nm, compared to 0.19 nm of Na^+.

Alkali metal carbonates, such as K_2CO_3, Na_2CO_3, and Li_2CO_3, can be alternatively used as the activating agent. The reaction involved is listed as follows:

$$M_2CO_3 \rightarrow M_2O + CO_2$$

$$M_2O + C \rightarrow 2M + CO$$

(where M = K, Na, or Li)

The remaining alkali metal and redundant carbonate salts are then removed by using HCl and subsequent distilled water wash.

According to Addoun's research, the radii of cations plays an important role in the development of porosity via alkali metal carbonates [90]. With the increase in cation radii, the pore volume increases as well. Besides, carbonate agents with larger alkali metal cations are usually thermally unstable, which promotes CO_2 bubbling.

$ZnCl_2$ is another promising activating agent for ACs synthesis. Different from alkali hydroxides and alkali metal carbonates, $ZnCl_2$ can be impregnated into the precursor and remove hydrogen and oxygen from the precursor with the formation of H_2O, resulting in the development of porosity. For example, Du *et al*. [46]

prepared activated carbon hollow fibers (ACHFs) from renewable ramie fibers through $ZnCl_2$ activation for the EDLC electrode. ACHFs calcined at 400 °C for 2 h exhibited an SSA of 2087 $m^2 g^{-1}$ with 38.1% carbon yield. In 6 M KOH electrolyte (aq. solution), the optimal ACHFs showed an impressive capacitance of 287 F g^{-1} under a specific current of 50 mA g^{-1}.

1.3.2.3 Electrochemical Activation

Sullivan *et al*. [91, 92] reported the surface activation of glassy carbon via electrochemical process. The activation consisted of applying a large positive potential in an aqueous electrolytic solution (e.g., 1 M H_2SO_4 aq. solution), during which a reduced thin layer of "activated" (partially oxidized to increase ion accessible surface area) glassy carbon was formed on the surface of the electrode. Besides the development of porous structure, in this process, surface functionalities were also obtained, which contributed to pseudocapacitance. The thickness of the active layer could be controlled in between <1 μm and around 100 μm. They found a strong correlation between the capacitance provided by the active layer and its thickness. An outstanding areal capacitance as high as 460 F cm^{-2} was achieved in this work. This activation method was followed by several works, with various results [93–97].

1.4 Various Forms of ACs as Supercapacitor Electrodes

Various forms of ACs have been synthesized, with different morphologies, porosities, and conductivities (Figure 1.2). In this section, we provide a brief review on the basic properties and pros/cons of each form of ACs as electrode material for supercapacitors.

1.4.1 Activated Carbon Powders

Commercial AC powders (Figure 1.2a) commonly offer SSA in the range of 700–2200 $m^2 g^{-1}$ and moderately high specific capacitance in the range of 70–200 F g^{-1} in aqueous and 50–120 F g^{-1} in organic electrolytes [70, 71, 100–102]. Furthermore, the recent developments in the synthesis of ACs having greatly enhanced specific capacitance (up to 250–300 F g^{-1} in aqueous, organic, and IL-based electrolytes) demonstrate that for a significant portion of EDLC applications, ACs may remain the material of choice [14, 29, 36, 44, 45, 55, 103, 104–107].

In order to minimize the ion diffusion distance within individual carbon particles, the particle size can be reduced to submicrons and even 10–30 nm range [108]. However, the use of porous nanoparticles reduces both the electrode density (and thus the energy density of the fabricated device) and the size of pores

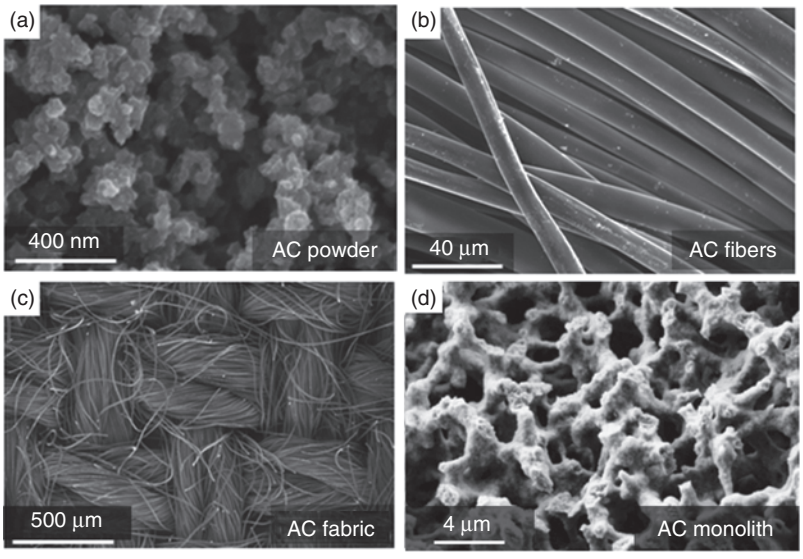

Figure 1.2 SEM images of (a) activated carbon powder [98] (Copyright © 2014 ACS Publications); (b) activated carbon fibers [69] (Copyright © 2012 Elsevier); (c) activated carbon fabric [69] (Copyright © 2012 Elsevier); and (d) macroporous activated carbon monoliths [99] (Copyright © 2007 Wiley). (All figures reproduced with permission.)

between the individual particles, which may ultimately lead to high ionic resistance in thick electrodes and reduced power density. In a systematic study performed on microporous carbon particles having different particle size but similar electrode mass per unit current collector area, small 20 nm size particles (also having small interparticle pore size), in fact, demonstrated power performance inferior to that of 600 nm particles [108]. In addition, with the exception of AC aerogels having interconnected nanoparticles, the major particle size reduction leads to a lower electrical conductivity of the electrodes (due to point contacts between individual particles), which may become significant enough to impact the EDLC's power characteristics. In addition, handling nanoparticles is difficult and they are difficult to pack densely, which reduces the volumetric device performance. Therefore, commercial EDLC electrodes continue to adopt microsized AC powder with large mesopores between the individual particles in the assembled and compressed electrodes.

1.4.2 Activated Carbon Films and Monoliths

Formation of EDLC electrodes from films and porous monoliths of ACs (Figure 1.2d) allows for a significant increase in their electrical conductivity (due to the elimination of both the nonconductive binder and the high resistance particle-to-particle point contacts) and, in cases when the pore volume in

monoliths is relatively small, their volumetric capacitance increases (due to the elimination of the large macropores between the particles) [33, 47, 57, 75, 76, 109]. For example, meso/microporous AC monoliths (1 mm thickness) produced by chemical activation (KOH) of mesophase pitch precursors and exhibiting SSA of up to 2650 $m^2 g^{-1}$ and surface area of micropores of up to 1830 $m^2 g^{-1}$ showed an outstanding initial capacitance of up to 334 $F g^{-1}$ in 1 M H_2SO_4 [47], which is one of the highest capacitance values reported for carbon materials. Nitrogen-doped macro/meso/microporous AC monoliths (cylindrical shape with up to 17 mm diameter) having a very moderate SSA of 772 $m^2 g^{-1}$ were recently shown to exhibit high specific capacitance of up to ~200 $F g^{-1}$ in 6 M KOH electrolyte [76]. In another recent study, S-containing macro/meso/microporous AC monoliths produced by physical (CO_2) activation of carbonized PDVB also demonstrated a specific capacitance of up to ~200 $F g^{-1}$ in 2 M H_2SO_4 electrolyte [33] (volumetric capacitance was not provided in the last two studies, but it is not expected to exceed ~40 $F cm^{-3}$ due to the presence of high content of macropores). A recent publication on patterned thin (1–3 μm) AC films reported a specific capacitance greater than 325 $F g^{-1}$ (>250 $F cm^{-3}$) in 1 M H_2SO_4 electrolyte [110].

1.4.3 Activated Carbon Fibers

AC fibers/fabrics (Figure 1.2c) commonly exhibit high electrical conductivity [39, 48, 51, 52, 54, 56, 59, 60, 63, 64, 111–116]. In contrast to monolithic electrodes, AC fabric electrodes could offer very high mechanical flexibility. Their higher power characteristics often originate from the smaller electrode thickness, high volume of macro/mesopores between the individual fibers, and higher electrical conductivity. Depending on the fiber diameter and the activation process utilized, the ion transport and the overall specific power of AC fiber-based EDLCs may vary in a broad range.

Apart from catalyst-grown carbon fibers, the smallest diameter AC fibers are produced by carbonization and activation of electrospun polymer solutions [48, 53, 54, 69, 77, 117–119]. The produced AC nanofiber electrodes exhibit an outstanding rate capability, but suffer from low density [48, 54]. In fact, the density of high-power AC fiber electrodes is often noticeably lower than that of AC powder electrodes, which leads to their lower volumetric capacitance. However, several studies have demonstrated very promising performance of dense AC fiber–based EDLCs. For example, pitch-derived carbon fiber electrodes (individual fiber diameter in the range of 2–30 μm) physically activated in an H_2O stream to moderately high SSA of 880 $m^2 g^{-1}$ while retaining high density (up to 0.8 $g cm^{-3}$) exhibited a specific capacitance of up to 112 $F g^{-1}$ (90 $F cm^{-3}$) in 1 M KCl electrolyte [59]. Chemical activation can similarly be used to control the density and porosity of carbon fibers. For example, chemically (KOH) activated mesophase-pitch–based carbon fibers showed an SSA increase from 510 to 2436 $m^2 g^{-1}$ upon increase in the KOH-to-C ratio from 1.5 to 4 [114]. The highest gravimetric capacitance in both ILs and tetraethyl ammonium tetrafluoroborate (TEATFB)-based organic

electrolytes (up to ~180 F g^{-1}) was achieved in the sample with the highest SSA, while the highest volumetric capacitance (up to ~88 F cm^{-3}) was achieved in moderately activated fibers with an SSA of 1143 m^2 g^{-1} [114].

Oxygen-containing plasma treatment of AC fibers was found to increase their SSA and specific capacitance in aqueous (0.5 M H_2SO_4) electrolytes [115, 116]. Interestingly, treatment in a pure O_2 atmosphere at moderate temperatures (~250 °C) did not significantly change the SSA, but introduced a higher content of C=O functional groups, which resulted in an increase in specific capacitance from 120 to 150 F g^{-1} in 1 M H_2SO_4 electrolyte, presumably owing to improved wetting and a higher contribution from pseudocapacitance produced by the introduced functional groups [66].

As summary to this section, the capacitive performance of AC-based electrodes reported by representative previous works is listed in Table 1.3.

1.5 Key Factors Determining the Electrochemical Performance of AC-Based Supercapacitors

The capacitive performance of AC-based supercapacitors is dependent on several key factors. Independent contributions of each factor could be challenging to separate, because most of these factors are strongly correlated. In this section, we summarize some of the most critical properties of ACs that affect their performance in cells.

1.5.1 Pore Size and Pore Size Distribution

According to the simplified equation for the capacitance calculation,

$$C = \frac{\varepsilon_0 \varepsilon_r A}{d}$$

The specific capacitance provided by carbons should be proportional to their SSA, often approximated as Brunauer–Emmett–Teller (BET) SSA. This linear dependence was indeed suggested in early studies for small S_{BET} values [19, 120], but the capacitance was found to be almost constant for S_{BET} at 1200–3000 m^2 g^{-1}. To explain this nonlinear behavior, the complicated pore structures of ACs need to be carefully characterized for better understanding of their electrochemical performance. ACs are highly porous materials with different types of pores, which are classified on the basis of their diameters: micropores(<2 nm), mesopores(2–50 nm), and macropores(>50 nm) [121]. Micropores play an essential role in the formation of electrical double layers. Shi [122] studied the relation between SSAs of microbeads and carbon fibers and their specific capacitances. It was suggested that the micropore surface is the most efficient in capacitance contribution (15–20 μF cm^{-2}), while capacitance from external (meso- and macropore) surface is dependent on the morphology

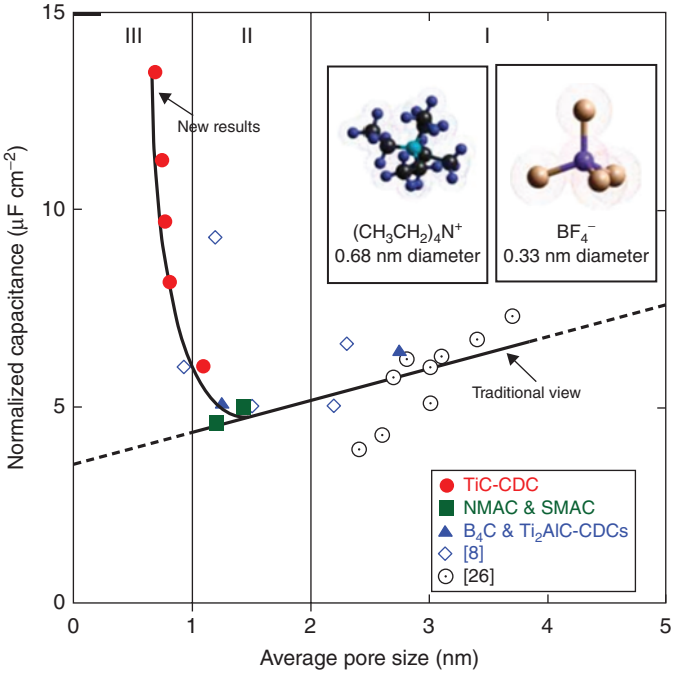

Figure 1.3 Carbon capacitance normalized by a BET specific surface area S_{BET} [123]. Anomalous capacitance increase happens when the pore size is reduced to less than 1 nm. (Reproduced with permission. Copyright © 2006 AAAS.)

of pores and surface functionalization. Since then, many works have confirmed the outstanding capacitive performance of micropores, especially ones with diameters <1 nm [123, 124]. Because electrolyte ions are generally shielded with solvent molecules, one may hypothesize that electrode pores that contribute capacitance should be at least larger than solvated ions. This theory was soon challenged by experimental observations [123, 125]. It was reported that pores that are smaller than solvated ions could still contribute capacitance [123]. In this case, the ion adsorption is realized by distortion of the solvation shell. This process provides a closer approach of the ion center to the electrode surface, which may result in anomalous increase in capacitance (Figure 1.3). The follow-up report applied solvent-free ionic liquid (IL) and revealed that the pore size leading to the maximum double-layer capacitance is very close to the ion size.

However, determination of the true SSA of AC with irregular shape of pores, reduction of the SSA during electrode processing, and the difference between the electrolyte ion accessible SSA and the SSA determined using gas sorption studies (N_2, Ar, CO_2) may induce significant discrepancies. Some of the smallest micropores accessible by gas molecules may not be accessible by ions and thus may not contribute to double-layer capacitance. Similar, ion intercalation might open some surface areas, which were previously inaccessible by gas molecules.

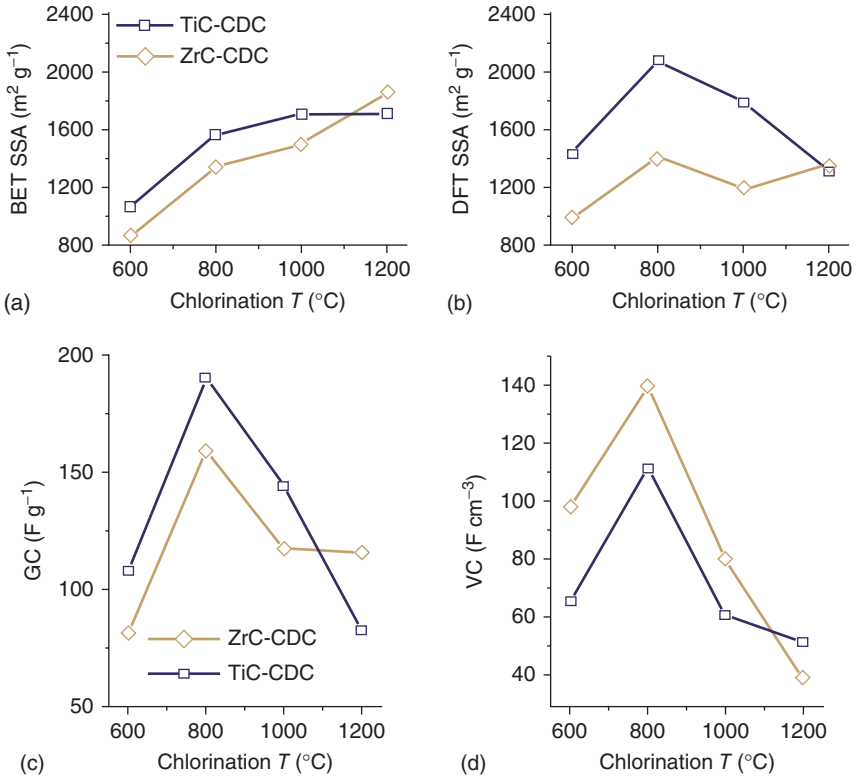

Figure 1.4 The evolution of (a) SSA_{BET}; (b) SSA_{DFT}; (c) gravimetric capacitance; and (d) volumetric capacitance of ZrC-CDC and TiC-CDC with chlorination temperature [124]. (Figure reproduced with permission. Copyright © 2006 Elsevier.)

The use of simplistic BET model may induce significant inaccuracies in SSA determination; and more advanced models for SSA and pore size distribution measurements are constantly being developed. For example, Ravikovitch and Neimark [126] developed a method for pore size distribution calculation on the basis of nonlocal density functional theory (NLDFT) of capillary condensation hysteresis in cylindrical pores. Chmiola *et al*. [124] compared the correlation of the specific capacitance of microporous carbide-derived carbons (CDCs) with their SSAs calculated on the basis of both BET and NLDFT, respectively. The researchers found a better correlation between the specific capacitance and DFT (density functional theory) SSA (SSA_{DFT}) than between the specific capacitance and BET SSA (SSA_{BET}) (Figure 1.4). Compared to BET method, DFT method allows a further comparison of double-layer capacitance with ultra-small micropores (<1 nm). On the basis of the analysis of pore size distribution, they found that the specific double-layer capacitance of CDC is mostly dependent on the surface area of the pores <2 nm (Figure 1.5).

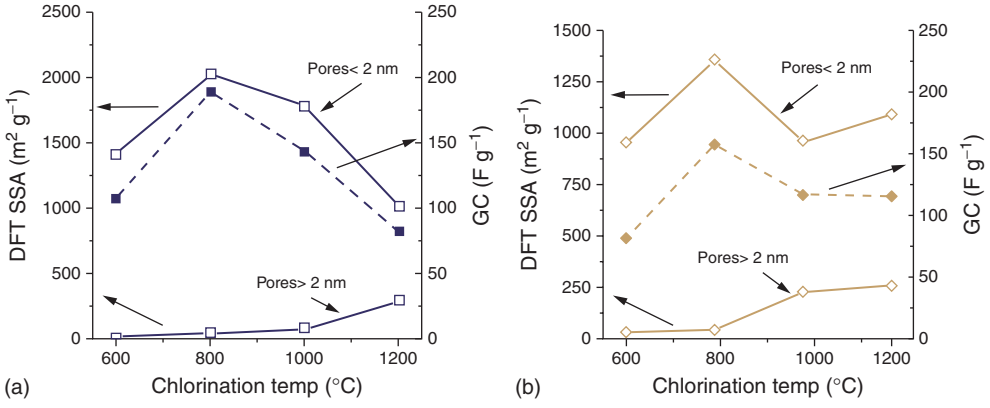

Figure 1.5 Micropore (<2 nm) and mesopore (>2 nm) surface area in comparison with gravimetric specific capacitance for (a) TiC-CDC and (b) ZrC-CDC [124]. A direct correlation between the micropore surface area and specific capacitance is evident. (Figure reproduced with permission. Copyright © 2006 Elsevier.)

While micropores lead to a higher volumetric and gravimetric capacitance than mesopores, electrodes with only micropores may suffer from the slow ion transport and the resulting high ionic resistance even under moderate current densities. Conversely, mesopores allow smooth entry for electrolyte ions and therefore enhance the capacitance and the power density of devices [87, 127–129]. Frackowiak *et al*. studied the coal-based ACs as electrode material for EDLC and found the optimized range of mesopore content within 20–50% [128]. This result, although still qualitative, shows that one needs to consider the balance in the pore size distribution of ACs for optimal EDLC performance in a given application. Chen *et al*. synthesized a series of micro- and mesoporous carbon materials with different SSA and pore size distribution by using different carbon sources and preparation methods. On the basis of the capacitive performance of these materials, they developed a general model for the estimation of capacitance, which is linearly proportional to "effective SSA," as determined by both the measured SSA and pore size distribution [130]. Further detailed models have been developed by taking pore curvature into consideration. Meunier *et al*. developed separate models for the calculation of micropore, mesopore, and macropore capacitances, respectively [131].

1.5.2
Pore Alignment

A recent study revealed the significant effect of pore alignment on the transport of ions within carbon nanopores [132]. In that work, zeolite-templated carbons were synthesized using low-pressure chemical vapor deposition (CVD). Identical micropore (<2 nm) size distributions with varying levels of pore alignment (as well as pore tortuosity) were achieved by manipulating the annealing conditions.

Electrochemical impedance spectroscopy measurements and cyclic voltammetry studies showed up to three orders of magnitude enhancements in the ion transport and frequency response accompanying the micropore alignment and a decrease in the concentration of obstacles for ion diffusion. This finding proves that other than introduction of mesopores as conducting paths, designing ACs with straight pores and low concentration of defects might be an alternative strategy for achieving rapid ion diffusion within individual electrode particles.

In response to the discovery of the essential role of pore alignment and optimization of pore size distribution for fast electrolyte diffusion and high power output of carbon EDLCs, researchers proposed various strategies to control the pore size and alignment of AC-based electrode materials. In order to achieve a higher SSA and eliminate bottle-neck pores, while uniformly enlarging the smallest micropores produced in the course of carbonization of organic precursors, several promising routes were proposed. According to one method, an equilibrium content of oxygen-containing functional groups is uniformly formed on the porous carbon surface during room temperature treatment in acids [32]. These groups together with the carbon atoms are later removed via heat treatment at 900 °C. Repetition of the process of uniform formation of chemisorbed oxygen functional groups, and subsequently removing them, allows for the uniform pore broadening needed to achieve the optimum pore size distribution [32]. In another study, an environmentally friendly low-temperature hydrothermal carbonization was utilized in order to introduce a network of uniformly distributed oxygen within the carbon structure in one step [14]. This material, produced from natural precursors (such as wood dust and potato starch), was then transformed into microporous carbons with high SSA of 2100–2450 $m^2 g^{-1}$ via simultaneous heat treatment (and thus uniform removal of the oxygen-containing functional groups from the internal material surface) and opening of closed and bottle-neck pores by activation. A very high specific capacitance of 140–210 $F g^{-1}$ was demonstrated in a TEATFB-based organic electrolyte [14]. Another efficient method for synthesis of carbons with controlled pore size distribution and alignment is the template method. In this method, highly ordered porous oxides, such as mesoporous silica are used as sacrificial template materials. Carbon precursors (sucrose solution, propylene, pitch, resin, etc.) are deposited inside the pores of the template and then carbonized. Then, the template is removed by dissolution in the hydrofluoric acid. The detailed discussion on highly ordered porous carbon is beyond the scope of this review, but readers are encouraged to refer to the representative works [133–137] on this important category of carbons.

1.5.3 Surface Functionalization

A variable amount of heteroatoms (oxygen, nitrogen, sulfur, etc.) can be added into the structure of carbon materials and functionalize their surfaces. Functionalized carbons can be synthesized by applying precursors containing heteroatoms [72, 138, 139] or posttreatment of carbons in heteroatom-enriched atmosphere

[66, 140]. The resulted functional groups can considerably enhance the gravimetric capacitance of electrodes by contributing additional pseudocapacitance, which involves rapid charge transfer reactions between the electrolyte and the functional moieties. The usually denser functionalized carbons, although with smaller SSA, provide a higher volumetric capacitance than highly porous intrinsic ACs. However, pseudocapacitance based on surface functionalization also suffers from intrinsic shortcomings, including relatively sluggish charge transfer process, serious self-discharge, and high leakage currents. These limitations are further discussed in Section 1.6.

1.5.4
Electrical Conductivity of the Electrode

To achieve high power output, charge carriers must move quickly and smoothly through electrodes, which requires high electrical conductivity. The electrical conductivity of AC-based electrodes strongly depends on the thermal treatment in the synthesis process, porous texture of the electrodes, and the content of heteroatoms [101].

Most carbon precursors are good insulators with a high content of σ- or sp^3-bonded carbon structures. During the thermal treatment at elevated temperatures, conductivity of the material is rapidly increased with the increasing content of sp^2-bonded conjugated carbon, because electrons associated with π-bonds are delocalized and become available as charge carriers [141]. The structural disorders and defects are healed to various extents, depending on the temperature applied for this process. Conductivity of carbon begins to increase at 600–700 °C, which corresponds to the range where loss of surface functionalities happens, until the formation of perfect crystalline graphite structure at over 2500 °C.

Generally, higher porosity leads to poorer electrical conductivity because of higher content of insulating voids. To enhance the electrical conductivity of highly porous ACs, several strategies could be applied, such as adding conductive agents, high-pressure packing of AC particles, and additional bonding network connecting particles.

In the previous section, we have discussed the enhancement of the capacitive performance of AC-based electrodes by surface functionalization. However, the effect of surface functionalization on the electric conductivity of the AC-based electrodes is largely negative. However, exceptions exist. For example, some functionalized carbons have higher density and, therefore, better electrical conductivity than porous intrinsic ACs [45]. Considering different categories of functionalities, oxygen functionalities, which preferentially form at the edge sites of graphite-like microcrystallites, increase the local barrier for electrons to transfer in between neighboring crystallite elements [142, 143]. Conversely, nitrogen functionalities are often grafted on basal planes of graphite crystallites, with an increase in local free electrons. As a result, proper amount of nitrogen doping increases the electrical conductivity of carbons. However, previous works

also reported aggravation of the capacitive performance of carbon materials from excess amount of nitrogen doping [144]. In summary, an optimized content of functionality is necessary for enhancement in capacitive performance of AC-based supercapacitors.

1.5.5 Electrolyte Selection

Electrolytes used in EDLCs may be divided into three classes: (i) aqueous (solutions of acids, bases, and salts), (ii) organic, and (iii) ILs. Each electrolyte has been intensively studied and widely acknowledged for its pros and cons [145]. ILs are nonflammable, are nontoxic, and offer a higher operating voltage than their counterparts. Serious shortcomings of ILs are their very high (often prohibitively high) current cost and relatively low ionic mobility at room temperature and below, which limits the charge/discharge rate of IL-based EDLCs. The advantages of using aqueous electrolytes include their very low cost, safety, and high ionic conductivity. Their disadvantages, however, include their low narrow electrochemical window and corrosion of EDLC electrodes observed at higher temperatures and voltages (particularly for acid-based electrolytes, such as H_2SO_4 solutions), which limits the cycle life of the EDLCs and contributes to self-discharge. Organic electrolytes are somewhat in between aqueous ones and ILs in terms of the price, voltage, and charge–discharge time. Organic electrolyte-based EDLCs offer cycle life in excess of 500 000 and are used in the majority of commercial EDLCs. In addition, EDLCs with organic electrolytes are much less flammable than Li-ion batteries.

Besides the selection of the electrolyte solvent, it is important to properly match the size of the electrolyte ions and the electrode pores of ACs. Aurbach *et al*. demonstrated that it was possible to selectively electroadsorb ions based on size [32, 146, 147]. They applied CVD of carbon on active porous carbon fibers to reduce the average pore size to 0.5–0.6 nm, which is in between the size of solvated monovalent (Na^+, ~0.4 nm) and bivalent cations (Ca^{2+}; Mg^{2+}, 0.6–0.7 nm) in the aqueous electrolytes applied. Electrodes with various average pore sizes were tested with different electrolytes in the three-electrode cyclic voltammograms (CVs). As a result (Figure 1.6), with $MgSO_4$ electrolyte, for larger pore sizes, which match the size of bivalent ions, rectangular shape of CV diagram was obtained; while for smaller pore sizes, negligible current was recorded in all potential ranges. Then, they replaced the cation and anion, respectively, with monovalent ions (Na^+ and Cl^-) and obtained asymmetric or even triangular CV diagrams, where the adsorption of much smaller monovalent ions contributes to much higher current than the opposite polarization. This result confirms the necessity of pores with proper size for the ion electroadsorption and insertion. Therefore, in manufacturing of AC-based supercapacitors, ion-sieving effect needs to be avoided for efficient access of electroadsorption sites to electrolyte ions.

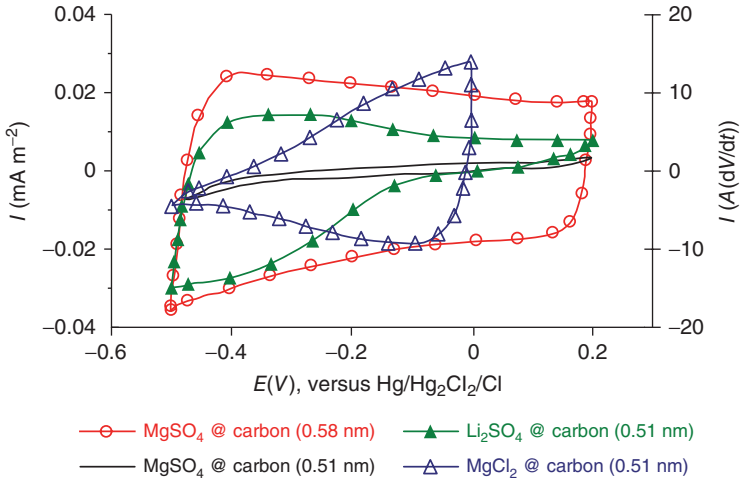

Figure 1.6 Cyclic voltammograms of activated carbon electrodes with an average pore size of 0.58 and 0.51 nm obtained in 0.1 M $MgSO_4$, Li_2SO_4, and $MgCl_2$ solutions [32, 146, 147]. The current is normalized by S_{BET}. (All data reproduced with permission. [146] Copyright © 2008 ACS Publications; [32] Copyright © 2006 Springer; [147] Copyright © 2009 ACS Publications.)

1.5.6 Understandings of Ion Adsorption in Porous Structure

With the goal of better understanding of ion adsorption behavior in polarized electrodes with different porous textures, several works relied on computer modeling and calculations for additional insights [148–152]. Realistic material systems are too complex for *ab initio* simulations. Many assumptions and simplifications were made as a prerequisite for meaningful calculations, each of which may significantly affect the obtained results.

Designing of systematic experiments with uncoupled parameters is also challenging. First, the key parameters determining the pore structures are strongly correlated. Carbon materials with different pore size distribution are also different in microstructure, pore shape, tortuosity, defects, and surface functionalities. Second, the conventional characterizations of porous texture depend on adsorption of gas molecules, which have different size than electrolyte ions. Third, there are no accurate models capable of deducing the SSA and pore size distribution from the commonly used gas sorption measurements in porous carbons with a realistic pore shape and size. The BET model is very simple and commonly used, but as previously discussed, it does not accurately represent gas sorption in microporous solids [153]. More advanced models, including the ones based on DFT calculations [154], are based on simplified pore shapes (such as infinitely long slit-shaped pores or cylindrical pores between perfect graphite pore walls), which are quite different from the realistic structure of microporous carbons.

Nuclear magnetic resonance (NMR) is a powerful tool that enables observations of the chemical and dynamic behaviors of the electrolyte ions present in the pores or adsorbed on the pore walls of porous structures [155–157]. Nucleus of certain elements involved in electrolyte ions that contain an odd number of protons or neutrons are often selected as the object of observation (e.g., ^{2}H, ^{10}B, ^{11}B, ^{19}F). The electron distribution of these nucleus varies with their local geometry (e.g., inside/outside pores), which results in distinguishable difference in the chemical shift. The number of electrolyte ions occupying a certain geometry is therefore proportional to the intensity of the corresponding chemical shift.

For example, Lee *et al*. [155] studied the adsorption of BF_4^- anion in ACs with different SSA and pore size via ^{11}B NMR. They labeled the possible states that could be occupied by ^{11}B by analysis on a nonpolarized, electrolyte-impregnated sample. Then, the *ex situ* ^{11}B NMR spectra at various charge stages were obtained and compared. As a result, they found a stronger adsorption of electrolyte ions on M500 carbon, which presented a smaller SSA but higher capacitances. To the contrary, although with a larger SSA, M3000 carbon showed a smaller capacitance, because of the rapid exchange between the adsorbed and free electrolyte ions. The fast ion exchange is attributed to the larger pore size of this carbon.

To get rid of the unintended discharge of the tested electrodes during the cell disassembly, which is necessary for *ex situ* tests, Wang *et al*. [156] proposed *in situ* NMR studies for EDLCs. The *in situ* measurement was made possible by a special configuration, in which the NMR coil was directly set up around a plastic bag containing cell assemblies. This approach enabled the real-time observation of migration of ions between the supercapacitor electrodes and change in the nature of ion binding to the electrode surface.

Deschamps *et al*. [158] applied ^{13}C and ^{11}B NMR studies to characterize the states of both electrode and electrolyte in ion adsorption between graphene layers, respectively. They found that the more disordered carbon shows a better capacitance and a better tolerance to more vigorous polarizations. Furthermore, they observed the unexpected excess of cations or anions between the graphene layers during polarization, which actually compensates the electronic charge carried by these layers.

Besides NMR-based methods, Boukhalfa *et al*. [159] proposed to use neutron scattering method to study ion adsorption in microporous carbons as a function of pore size and applied potential. The researchers showed that by monitoring changes in the distribution of either hydrogen or boron (which could be present in either electrolyte solvent molecules or ions or both) in pores of different size, one can elucidate where the ion adsorption takes place. In their first work, they showed that depending on the solvent properties and the solvent–pore walls interactions, either enhanced or diminished ion adsorption may take place in sub-nanometer pores. The reported tests have been performed in electrolytes based on the solution of H_2SO_4 in H_2O and D_2O (heavy water). In the case of an H_2O solvent, under the application of −0.6 V, the scattering intensity increases by ~6% (Figure 1.7a), which represents the H enrichment of 6% within the relatively large pores. The smallest pores ($Q > 0.5$ Å^{-1}) exhibit even higher ion adsorption

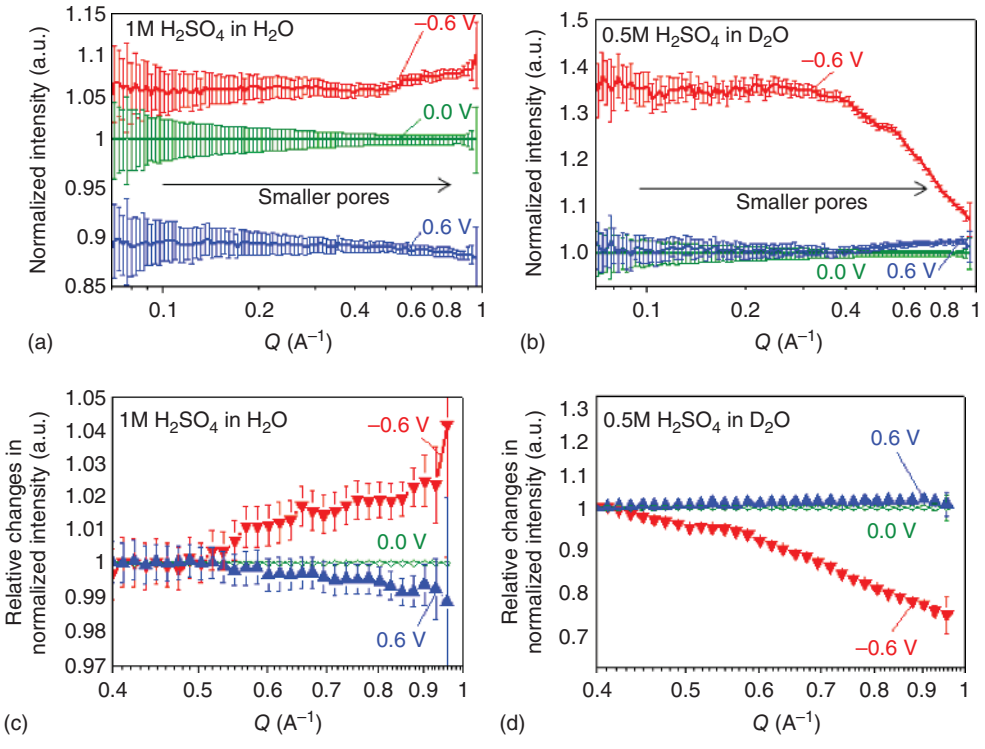

Figure 1.7 *In situ* neutron scattering experiments on AC electrodes immersed into H_2O-based (a,c) and D_2O-based (b,d) electrolytes under the application of a potential between the working and counter electrodes: (a,b) SANS profiles normalized by the 0 V one, (b,d) relative changes in the intensity of the normalized SANS profiles [159]. (Figure reproduced with permission. Copyright © 2013 Wiley.)

capacity, as manifested by higher H concentration in such pores at negative potentials and lower H concentration at positive potentials. In Figure 1.5c showing the relative changes in the normalized scattering intensities, such an effect can be seen most clearly. In case of a D_2O solvent (Figure 1.7b,d), the negative polarization increases the neutron scattering intensity more dramatically because the scattering contrast between carbon and D_2O is much smaller than that between carbon and H_2O. Under the application of −0.6 V, the concentration of H increases by ~35% in large pores. However, in sharp contrast to H_2O solvent studies (Figure 1.7c), cation adsorption is significantly reduced in the smallest pores ($Q > 0.4$ Å^{-1}) in case of a D_2O solvent (Figure 1.7d). By analyzing the adsorption of D_2O and H_2O vapors, it was found that a significant portion of the smallest pores ($Q > 0.3$ Å^{-1}) is not filled with D_2O and not accessible by electrolyte. The higher energy cost of maintaining a stronger deuterium bond network (compared to a protium bond network) at the sub-nanometers proximity to the hydrophobic carbon surface was proposed to be responsible for

the formation of D_2O-based electrolyte depletion regions and for the dramatic difference between the electroadsorption of D_2O- and H_2O-based electrolyte ions in the smallest carbon nanopores. In contrast to other studies, in which the impact of pore size was studied by analyzing completely different carbons, neutron scattering experiments allow unambiguous observation of the different ion adsorption in various pores of the same material. The reported methodology may become instrumental in clarifying the existing controversies. It may also contribute to the formulation of the predictive models of ion adsorption.

1.5.7 Quantum Capacitance of Carbon and Doping

Early studies on graphite-based electrochemical capacitors revealed a peculiar phenomenon [160–163]. The interfacial capacitance provided by graphite electrodes is unusually small compared with that of metal electrodes with identical dimensions. Furthermore, the capacitance of graphite performs a V-shaped dependence on the applied voltage. This phenomenon was interpreted by Gerischer as a low density of electronic energy states (DOSs) around the Fermi level of graphite [164]. In other words, the Fermi level of semiconductive electrodes such as graphite cannot accommodate as many charge carriers as conductive electrodes, such as metals. When a graphite-based electrode is charged, electrons are filled in the negative side and depleted from the positive side. Energy of electrons on both sides deviate from the Fermi level, which results in an extra voltage change over the Galvani potential difference. The effect of quantum capacitance is equivalent to an extra capacitor in series with the original capacitor: the smaller capacitance dominates the total value. For in-depth understanding, great efforts have been made on the accurate and intuitive measurement of quantum capacitance effect. Graphene and semiconductive carbon nanotubes (CNTs) are often selected as the research objects because of their well-defined band structures. Details on the characterization of quantum capacitance are beyond the scope of this chapter, but interested readers are encouraged to refer to representative studies [165–167].

To diminish the reduction in capacitance of semiconductive electrodes caused by the quantum capacitance effect, researchers intended to dope heteroatoms in the electrodes to increase the density of energy states. For example, Jang *et al*. [168] modified the surface of double-walled CNTs via oxidation using nitric acid. Despite of their smaller SSAs, the oxidized CNTs exhibited higher capacitances than pristine CNTs in both aqueous and nonaqueous systems. This could be explained, unfortunately, by multiple factors, including pseudocapacitance contribution, changes in the electrolyte/carbon surface energy, changes in the electrolyte desolvation behavior, in addition to possible changes in the carbon DOS. Zhang *et al*. [169] enhanced capacitance of graphene via nitrogen-doping, which may similarly be caused by multiple factors. With 2.3 at% nitrogen-doping, the area-normalized capacitance of graphene increased from 6 to 22 $\mu F\ cm^{-2}$.

1.6 Self-discharge of ACs-Based Supercapacitors

For some of the supercapacitors applications, such as alternative and emergency power supply, long shelf-life and low self-discharge of supercapacitors are required. Unfortunately, AC-based supercapacitors are prone to a gradual decrease in voltage during long-term storage. This spontaneous (thermodynamically favored) process is named "self-discharge" and is known to depend on the initial voltage, purity of carbon, and electrolyte as well as on electrolyte acidity. There are several possible reasons for self-discharge. First, when the electrode is polarized to a potential that exceeds the electrochemical window of the electrolyte, the decomposition of the electrolyte happens at the electrode/electrolyte interface. This Faradic process reduces the cell potential continuously until the electrode potential falls into the electrochemical window of the electrolyte or the electrolyte is totally consumed. Besides, this process usually produces gases, which may block the pores of the electrodes and the separator and even induce a separation of individual particles within the electrode. This, in turn, may result in the capacitance fading (due to the reduction of accessible SSA of the electrodes) and in the reduction of power performance (due to the increased separator resistance). It also leads to an increase in the ESR. Second, some redox-active impurities on the surface of the electrodes or in the electrolytes (such as O_2, H_2O, H_2O_2, metal ions, and others) may be involved in undesirable (parasitic) Faradic processes, which may consume the charge stored in an EDLC or lead to electrolyte degradation.

Other than impurities, the intentionally grafted surface functionalities on carbon electrodes are also claimed to be responsible for the capacitance fading [120, 170]. Although these surface functionalities contribute to pseudocapacitance, they are often thermodynamically unstable within the potential range and either readily decompose themselves or induce electrolyte decomposition, thus producing various gases (such as NO_2, SO_2, SO_3) [101].

Some researchers speculate that selected functional groups on carbon may possibly be stable in the operating potential range. Unfortunately, selective functionalization of carbon surface only with some particular functional groups is a challenging task. Furthermore, commonly available surface chemistry characterization tools (Fourier transform infrared spectroscopy (FTIR), X-ray photoelectron spectroscopy (XPS), chemical titration, etc.) have difficulties to unambiguously interpret the presence of particular functional groups because the peaks corresponding to different groups are relatively broad and their position may be sufficiently close. Currently, no comprehensive understanding exists on the specific contributions of various functional groups to either the desirable or undesirable performance characteristics of EDLCs in various organic and aqueous electrolytes. So far, the feasibility of the concept to induce pseudocapacitance on carbon without penalties in leakage and degradation is unclear [171]. We notice in our studies that the degree of leakage current may depend on both the

presence of functional groups in carbon and the electrolyte utilized (pH-neutral aqueous electrolytes commonly induce lower leakage) [72].

Successful formation of stable functional groups on carbon that do not induce leakage has not been achieved in commercial devices. Carbon electrodes utilized in commercial EDLCs are nonfunctionalized and purified to a high degree. Historically, improvements in the purification procedures allowed commercial devices to increase their cycle life from tens of thousands to several million cycles. In addition, such improvements in the purification of carbons and electrolytes allowed EDLC manufacturers to reduce the characteristic self-discharge time constant from a few hours to months (at room temperature).

Finally, besides surface impurities and functionalities, self-discharge may also be attributed to Ohmic leakage from unintended interelectrode contacts or leaky bipolar electrodes.

Several theories have been developed to distinguish the mechanism that causes self-discharge of a supercapacitor via electrochemical characterizations. According to Conway's model [172, 173], self-discharge processes that follow different mechanisms would perform different potential fading rate. Other than this work, studies on proper modeling and simulation of self-discharge have been performed by many [63, 174–176], including some supplement to Conway's model. For example, Kaus *et al.* [174] suggested that charge distribution at an open circuit may contribute to self-discharge. According to one recently proposed model by Yushin *et al.* [72], functional groups on the AC electrode surface locally change pH in their vicinity. Because electrolyte stability is pH dependent, higher pH at local areas of the cathode (positive electrode) may lead to electrolyte oxidation even when the electrolyte should generally be stable at the cathode potential. Similarly, lower pH at local areas of the anode (negative electrode) may lead to electrolyte reduction [72].

1.7 Summary

In this chapter, we reviewed some of the recent studies of syntheses and applications of various nanostructured ACs as electrode materials for supercapacitors and then discussed the related structure–property–performance relationships. The impact of the activation processes and selection of precursors have been reviewed and discussed as well. For AC-based EDLCs, electrochemical performance is determined by a broad range of AC properties, such as the pore size distribution, pore alignment, and tortuosity; the presence of defects and functional groups; carbon density; carbon doping; density of states in carbon; and electrolyte/electrode interfacial energy, to name a few. Surface functionalities add extra pseudocapacitance but may result in sluggish kinetics and self-discharge from side-reactions involving electrolyte decomposition and redox reactions with functional groups. Recently introduced advanced characterization and modeling efforts may help scientists to deepen their understanding of ion electrosorption

in nanopores of ACs. We hope the discussions in this chapter may serve as guidance for future efforts in research, development, and production of novel carbon materials for advanced supercapacitors with improved performance.

References

1. Laine, J. and Yunes, S. (1992) *Carbon*, **30**, 601–604.
2. Daud, W.M.A.W. and Ali, W.S.W. (2004) *Bioresour. Technol.*, **93**, 63–69.
3. Yang, K., Peng, J., Srinivasakannan, C., Zhang, L., Xia, H., and Duan, X. (2010) *Bioresour. Technol.*, **101**, 6163–6169.
4. Hu, Z. and Srinivasan, M. (1999) *Microporous Mesoporous Mater.*, **27**, 11–18.
5. Kumagai, S., Ishizawa, H., and Toida, Y. (2010) *Fuel*, **89**, 365–371.
6. Azevedo, D., Araujo, J., Bastos-Neto, M., Torres, A.E.B., Jaguaribe, E.F., and Cavalcante, C.L. (2007) *Microporous Mesoporous Mater.*, **100**, 361–364.
7. Hayashi, J.I., Horikawa, T., Takeda, I., Muroyama, K., and Nasir Ani, F. (2002) *Carbon*, **40**, 2381–2386.
8. Hu, Z. and Srinivasan, M. (2001) *Microporous Mesoporous Mater.*, **43**, 267–275.
9. Marsh, H. (2001) *Activated Carbon Compendium: A Collection of Papers from the Journal Carbon 1996–2000*, Elsevier, Amsterdam, New York.
10. Subramanian, V., Luo, C., Stephan, A.M., Nahm, K.S., Thomas, S., and Wei, B.Q. (2007) *J. Phys. Chem. C*, **111**, 7527–7531.
11. Wei, L. and Yushin, G. (2011) *Carbon*, **49**, 4830–4838.
12. Wei, L. and Yushin, G. (2011) *J. Power Sources*, **196**, 4072–4079.
13. Li, Q.Y., Wang, H.Q., Dai, Q.F., Yang, J.H., and Zhong, Y.L. (2008) *Solid State Ionics*, **179**, 269–273.
14. Wei, L., Sevilla, M., Fuertes, A.B., Mokaya, R., and Yushin, G. (2011) *Adv. Energy Mater.*, **1**, 356–361.
15. Balathanigaimani, M.S., Shim, W.G., Lee, M.J., Kim, C., Lee, J.W., and Moon, H. (2008) *Electrochem. Commun.*, **10**, 868–871.
16. Kierzek, K., Frackowiak, E., Lota, G., Gryglewicz, G., and Machnikowski, J. (2004) *Electrochim. Acta*, **49**, 515–523.
17. Zhai, D., Li, B., Du, H., Wang, G., and Kang, F. (2011) *J. Solid State Electrochem.*, **15**, 787–794.
18. Rufford, T.E., Hulicova-Jurcakova, D., Khosla, K., Zhu, Z.H., and Lu, G.Q. (2010) *J. Power Sources*, **195**, 912–918.
19. Lozano-Castello, D., Cazorla-Amoros, D., Linares-Solano, A., Shiraishi, S., Kurihara, H., and Oya, A. (2003) *Carbon*, **41**, 1765–1775.
20. Xu, B., Chen, Y.F., Wei, G., Cao, G.P., Zhang, H., and Yang, Y.S. (2010) *Mater. Chem. Phys.*, **124**, 504–509.
21. Rufford, T.E., Hulicova-Jurcakova, D., Zhu, Z., and Lu, G.Q. (2008) *Electrochem. Commun.*, **10**, 1594–1597.
22. Li, X., Han, C., Chen, X., and Shi, C. (2010) *Microporous Mesoporous Mater.*, **131**, 303–309.
23. Wang, R., Wang, P., Yan, X., Lang, J., Peng, C., and Xue, Q. (2012) *ACS Appl. Mater. Interfaces*, **4**, 5800–5806.
24. Lee, S.G., Park, K.H., Shim, W.G., Balathanigaimani, M.S., and Moon, H. (2011) *J. Ind. Eng. Chem.*, **17**, 450–454.
25. Juntao Zhang, L.G., Kang, S., Jianchun, J., and Xiaogang, Z. (2012) *J. Solid State Electrochem.*, **16**, 3355–3362.
26. Elmouwahidi, A., Zapata-Benabithe, Z., Carrasco-Marin, F., and Moreno-Castilla, C. (2012) *Bioresour. Technol.*, **111**, 185–190.
27. Ding, L., Wang, Z., Li, Y., Du, Y., Liu, H., and Guo, Y. (2012) *Mater. Lett.*, **74**, 111–114.
28. Li, Z., Zhang, L., Amirkhiz, B.S., Tan, X., Xu, Z., Wang, H., Olsen, B.C., Holt, C.M.B., and Mitlin, D. (2012) *Adv. Energy Mater.*, **2**, 431–437.
29. Wei, L., Sevilla, M., Fuertes, A.B., Mokaya, R., and Yushin, G. (2012) *Adv. Funct. Mater.*, **22** (4), 827–834.

30. Yan, J., Wei, T., Qiao, W., Fan, Z., Zhang, L., Li, T., and Zhao, Q. (2010) *Electrochem. Commun.*, **12**, 1279–1282.
31. Xiang, X., Liu, E., Li, L., Yang, Y., Shen, H., Huang, Z., and Tian, Y. (2011) *J. Solid State Electrochem.*, **15**, 579–585.
32. Eliad, L., Pollak, E., Levy, N., Salitra, G., Soffer, A., and Aurbach, D. (2006) *Appl. Phys. A*, **82**, 607–613.
33. Hasegawa, G., Aoki, M., Kanamori, K., Nakanishi, K., Hanada, T., and Tadanaga, K. (2011) *J. Mater. Chem.*, **21**, 2060–2063.
34. Kim, K.-S. and Park, S.-J. (2012) *Microporous Mesoporous Mater.*, **163**, 140–146.
35. Wang, F., Guo, S., Chen, H., Ren, H., Wang, R., and Pan, X. (2012) *J. Solid State Electrochem.*, **16** (10), 3355–3362.
36. Hulicova-Jurcakova, D., Seredych, M., Lu, G.Q., and Bandosz, T.J. (2009) *Adv. Funct. Mater.*, **19**, 438–447.
37. Ma, Z.X., Kyotani, T., and Tomita, A. (2000) *Phys. Chem. Chem. Phys.*, **2**, 2365–2366.
38. Endo, M., Kim, Y.J., Maeda, T., Koshiba, K., Katayam, K., and Dresselhaus, M.S. (2001) *J. Mater. Res.*, **16**, 3402–3410.
39. Endo, M., Maeda, T., Takeda, T., Kim, Y.J., Koshiba, K., Hara, H., and Dresselhaus, M.S. (2001) *J. Electrochem. Soc.*, **148**, A910.
40. Alonso, A., Ruiz, V., Blanco, C., Santamaría, R., Granda, M., Menéndez, R., and de Jager, S.G.E. (2006) *Carbon*, **44**, 441–446.
41. Huang, C.-W., Hsieh, C.-T., Kuo, P.-L., and Teng, H. (2012) *J. Mater. Chem.*, **22**, 7314.
42. Sudaryanto, Y., Hartono, S., Irawaty, W., Hindarso, H., and Ismadji, S. (2006) *Bioresour. Technol.*, **97**, 734–739.
43. Zhao, S., Wang, C.-Y., Chen, M.-M., Wang, J., and Shi, Z.-Q. (2009) *J. Phys. Chem. Solids*, **70**, 1256–1260.
44. Raymundo-Pinero, E., Cadek, M., and Beguin, F. (2009) *Adv. Funct. Mater.*, **19**, 1032–1039.
45. Raymundo-Piñero, E., Leroux, F., and Béguin, F. (2006) *Adv. Mater.*, **18**, 1877–1882.
46. Du, X., Zhao, W., Wang, Y., Wang, C., Chen, M., Qi, T., Hua, C., and Ma, M. (2013) *Bioresour. Technol.*, **149**, 31–37.
47. Ruiz, V., Blanco, C., Santamaria, R., Ramos-Fernandez, J.M., Martinez-Escandell, M., Sepulveda-Escribano, A., and Rodriguez-Reinoso, F. (2009) *Carbon*, **47**, 195–200.
48. Kim, B.-H., Yang, K.S., Woo, H.-G., and Oshida, K. (2011) *Synth. Met.*, **161**, 1211–1216.
49. Kim, Y.J., Horie, Y., Ozaki, S., Matsuzawa, Y., Suezaki, H., Kim, C., Miyashita, N., and Endo, M. (2004) *Carbon*, **42**, 1491–1500.
50. Bodugöz-Sentürk, H. and Güven, O. (2011) *Radiat. Phys. Chem.*, **80**, 153–158.
51. Endo, M., Kim, Y.J., Takeda, T., Maeda, T., Hayashi, T., Koshiba, K., Hara, H., and Dresselhaus, M.S. (2001) *J. Electrochem. Soc.*, **148**, A1135–A1140.
52. Seo, M.-K. and Park, S.-J. (2009) *Mater. Sci. Eng., B*, **164**, 106–111.
53. Chen, H., Wang, F., Tong, S., Guo, S., and Pan, X. (2012) *Appl. Surf. Sci.*, **258**, 6097–6102.
54. Kim, C. (2005) *J. Power Sources*, **142**, 382–388.
55. Han, S.-J., Kim, Y.-H., Kim, K.-S., and Park, S.-J. (2012) *Curr. Appl Phys.*, **12**, 1039–1044.
56. Babel, K. and Jurewicz, K. (2004) *J. Phys. Chem. Solids*, **65**, 275–280.
57. Taer, M.D.E., Talib, I.A., Awitdrus, A., Hashmi, S.A., and Umar, A.A. (2011) *Int. J. Electrochem. Sci.*, **6**, 3301–3315.
58. Guo, S.L., Wang, F., Chen, H., Ren, H., Wang, R.S., and Pan, X.M. (2012) *J. Solid State Electrochem.*, **16**, 3355–3362.
59. Nakagawa, H., Shudo, A., and Miura, K. (2000) *J. Electrochem. Soc.*, **147**, 38–42.
60. Kim, Y.J., Endo, M., Maeda, T., Koshiba, K., and Katayam, K. (2001) *J. Mater. Res.*, **16**, 3402–3410.
61. Weng, T.-C. and Teng, H. (2001) *J. Electrochem. Soc.*, **148**, A368.
62. Chun, S.-E. and Whitacre, J.F. (2012) *Electrochim. Acta*, **60**, 392–400.
63. Zhang, Q., Rong, J.P., Ma, D.S., and Wei, B.Q. (2011) *Energy Environ. Sci.*, **4**, 2152–2159.

64. Hung, K.S., Masarapu, C., Ko, T.H., and Wei, B.Q. (2009) *J. Power Sources*, **193**, 944–949.
65. Liu, E., Xiang, X., Huang, Z., Shen, H., Tian, Y., Xiao, C., Yang, J., and Mao, Z. (2011) *J. Solid State Electrochem.*, **15**, 2667–2674.
66. Hsieh, C.T. and Teng, H. (2002) *Carbon*, **40**, 667–674.
67. Zhang, X., Wang, X., Jiang, L., Wu, H., Wu, C., and Su, J. (2012) *J. Power Sources*, **216**, 290–296.
68. Teng, H., Chang, Y.-J., and Hsieh, C.-T. (2001) *Carbon*, **39**, 1981.
69. Ma, C., Song, Y., Shi, J., Zhang, D., Zhong, M., Guo, Q., and Liu, L. (2012) *Mater. Lett.*, **76**, 211–214.
70. Taberna, P.L., Simon, P., and Fauvarque, J.F. (2003) *J. Electrochem. Soc.*, **150**, A292–A300.
71. Gamby, J., Taberna, P.L., Simon, P., Fauvarque, J.F., and Chesneau, M. (2001) *J. Power Sources*, **101**, 109–116.
72. Gu, W., Sevilla, M., Magasinski, A., Fuertes, A.B., and Yushin, G. (2013) *Energy Environ. Sci.*, **6**, 2465.
73. Nandhini, R., Mini, P.A., Avinash, B., Nair, S.V., and Subramanian, K.R.V. (2012) *Mater. Lett.*, **87**, 165–168.
74. Puziy, A.M., Hulicova-Jurcakova, D., Poddubnaya, O.I., Suarez-Garcia, F., Tascon, J.M.D., and Lu, G.Q. (2009) *J. Am. Chem. Soc.*, **131** (14), 5026–5027.
75. Carriazo, D., Picó, F., Gutiérrez, M.C., Rubio, F., Rojo, J.M., and del Monte, F. (2010) *J. Mater. Chem.*, **20**, 773.
76. Hao, G.P., Mi, J., Li, D., Qu, W.H., Wu, T.J., Li, W.C., and Lu, A.H. (2011) *New Carbon Mater.*, **26**, 197–203.
77. Kim, C., Park, S.-H., Lee, W.-J., and Yang, K.-S. (2004) *Electrochim. Acta*, **50**, 877–881.
78. Jänes, A., Kurig, H., and Lust, E. (2007) *Carbon*, **45**, 1226–1233.
79. Yang, H., Yoshio, M., Isono, K., and Kuramoto, R. (2002) *Electrochem. Solid-State Lett.*, **5**, A141.
80. Bouchelta, C., Medjram, M.S., Bertrand, O., and Bellat, J.-P. (2008) *J. Anal. Appl. Pyrolysis*, **82**, 70–77.
81. Aworn, A., Thiravetyan, P., and Nakbanpote, W. (2008) *J. Anal. Appl. Pyrolysis*, **82**, 279–285.
82. Lillo-Ródenas, M., Cazorla-Amorós, D., and Linares-Solano, A. (2003) *Carbon*, **41**, 267–275.
83. Gonzalez-Serrano, E., Cordero, T., Rodriguez-Mirasol, J., and Rodriguez, J. (1997) *Ind. Eng. Chem. Res.*, **36**, 4832–4838.
84. Evans, M., Halliop, E., and MacDonald, J. (1999) *Carbon*, **37**, 269–274.
85. Wang, J. and Kaskel, S. (2012) *J. Mater. Chem.*, **22**, 23710–23725.
86. Zhang, L.L. and Zhao, X. (2009) *Chem. Soc. Rev.*, **38**, 2520–2531.
87. Frackowiak, E. (2007) *Phys. Chem. Chem. Phys.*, **9**, 1774–1785.
88. Zhai, Y., Dou, Y., Zhao, D., Fulvio, P.F., Mayes, R.T., and Dai, S. (2011) *Adv. Mater.*, **23**, 4828–4850.
89. Hwang, H.-R., Choi, W.-J., Kim, T.-J., Kim, J.-S., and Oh, K.-J. (2008) *J. Anal. Appl. Pyrolysis*, **83**, 220–226.
90. Addoun, A., Dentzer, J., and Ehrburger, P. (2002) *Carbon*, **40**, 1140–1143.
91. Sullivan, M., Schnyder, B., Bärtsch, M., Alliata, D., Barbero, C., Imhof, R., and Kötz, R. (2000) *J. Electrochem. Soc.*, **147**, 2636–2643.
92. Sullivan, M.G., Kötz, R., and Haas, O. (2000) *J. Electrochem. Soc.*, **147**, 308–317.
93. Thiagarajan, S., Tsai, T.-H., and Chen, S.-M. (2009) *Biosens. Bioelectron.*, **24**, 2712–2715.
94. Beidaghi, M., Chen, W., and Wang, C. (2011) *J. Power Sources*, **196**, 2403–2409.
95. Braun, A., Bärtsch, M., Merlo, O., Schnyder, B., Schaffner, B., Kötz, R., Haas, O., and Wokaun, A. (2003) *Carbon*, **41**, 759–765.
96. Xu, H., Fan, X., Lu, Y., Zhong, L., Kong, X., and Wang, J. (2010) *Carbon*, **48**, 3300–3303.
97. Fan, X., Lu, Y., Xu, H., Kong, X., and Wang, J. (2011) *J. Mater. Chem.*, **21**, 18753–18760.
98. Zhao, Y., Liu, M., Gan, L., Ma, X., Zhu, D., Xu, Z., and Chen, L. (2014) *Energy Fuel*, **28**, 1561–1568.
99. Fan, L.Z., Hu, Y.S., Maier, J., Adelhelm, P., Smarsly, B., and Antonietti, M. (2007) *Adv. Funct. Mater.*, **17**, 3083–3087.

100. Simon, P. and Gogotsi, Y. (2008) *Nat. Mater.*, **7**, 845–854.
101. Frackowiak, E. and Beguin, F. (2001) *Carbon*, **39**, 937–950.
102. Azaïs, P., Duclaux, L., Florian, P., Massiot, D., Lillo-Rodenas, M.-A., Linares-Solano, A., Peres, J.-P., Jehoulet, C., and Béguin, F. (2007) *J. Power Sources*, **171**, 1046–1053.
103. Hulicova-Jurcakova, D., Kodama, M., Shiraishi, S., Hatori, H., Zhu, Z.H., and Lu, G.Q. (2009) *Adv. Funct. Mater.*, **19**, 1800–1809.
104. Liang, Y.Y., Schwab, M.G., Zhi, L.J., Mugnaioli, E., Kolb, U., Feng, X.L., and Mullen, K. (2010) *J. Am. Chem. Soc.*, **132**, 15030–15037.
105. Balducci, A., Dugas, R., Taberna, P.L., Simon, P., Plée, D., Mastragostino, M., and Passerini, S. (2007) *J. Power Sources*, **165**, 922–927.
106. Zhang, X., Sun, X., Zhang, H., Zhang, D., and Ma, Y. (2012) *J. Solid State Electrochem.*, **16** (8), 2597–2603
107. Timperman, L., Skowron, P., Boisset, A., Galiano, H., Lemordant, D., Frackowiak, E., Beguin, F., and Anouti, M. (2012) *Phys. Chem. Chem. Phys.*, **14**, 8199–8207.
108. Portet, C., Yushin, G., and Gogotsi, Y. (2008) *J. Electrochem. Soc.*, **155** (7), A531–A536.
109. Garcia-Gomez, A., Miles, P., Centeno, T.A., and Rojo, J.M. (2010) *Electrochim. Acta*, **55**, 8539–8544.
110. Wei, L., Nitta, N., and Yushin, G. (2013) *ACS Nano*, **7**, 6498–6506.
111. Lewandowski, A., Olejniczak, A., Galinski, M., and Stepniak, I. (2010) *J. Power Sources*, **195**, 5814–5819.
112. McDonough, J.R., Choi, J.W., Yang, Y., La Mantia, F., Zhang, Y.G., and Cui, Y. (2009) *Appl. Phys. Lett.*, **95** (24), 243109.
113. Xu, B., Wu, F., Chen, R., Cao, G., Chen, S., and Yang, Y. (2010) *J. Power Sources*, **195**, 2118–2124.
114. Kim, Y.J., Matsuzawa, Y., Ozaki, S., Park, K.C., Kim, C., Endo, M., Yoshida, H., Masuda, G., Sato, T., and Dresselhausc, M.S. (2005) *J. Electrochem. Soc.*, **152**, A710–A715.
115. Okajima, K., Ohta, K., and Sudoh, M. (2005) *Electrochim. Acta*, **50**, 2227–2231.
116. Ishikawa, M., Sakamoto, A., Morita, M., Matsuda, Y., and Ishida, K. (1996) *J. Power Sources*, **60**, 233–238.
117. Liu, J., Dayal, P., Kumar, S., and Kyu, T. (2007) *Macromolecules*, **40** (21), 7689–7694.
118. Wang, T. and Kumar, S. (2006) *J. Appl. Polym. Sci.*, **102**, 1023–1029.
119. Rahatekar, S.S., Rasheed, A., Jain, R., Zammarano, M., Koziol, K.K., Windle, A.H., Gilman, J.W., and Kumar, S. (2009) *Polymer*, **50**, 4577–4583.
120. Hiratsuka, K., Morimoto, T., Sanada, Y., and Kurihara, K. (1996) *J. Power Sources*, **60**, 239–247.
121. Conway, B.E. (1999) *Electrochemical Supercapacitors*, Kluwer Academic/Plenum Publishers, New York.
122. Shi, H. (1996) *Electrochim. Acta*, **41**, 1633.
123. Chmiola, J., Yushin, G., Gogotsi, Y., Portet, C., Simon, P., and Taberna, P.-L. (2006) *Science*, **313**, 1760–1763.
124. Chmiola, J., Yushin, G., Dash, R., and Gogotsi, Y. (2006) *J. Power Sources*, **158**, 765–772.
125. Largeot, C., Portet, C., Chmiola, J., Taberna, P.L., Gogotsi, Y., and Simon, P. (2008) *J. Am. Chem. Soc.*, **130** (9), 2730–2731.
126. Ravikovitch, P.I. and Neimark, A.V. (2001) *Colloids Surf., A*, **187**, 11–21.
127. Vaquero, S., Díaz, R., Anderson, M., Palma, J., and Marcilla, R. (2012) *Electrochim. Acta*, **86**, 241–247.
128. Gryglewicz, G., Machnikowski, J., Lorenc-Grabowska, E., Lota, G., and Frackowiak, E. (2005) *Electrochim. Acta*, **50**, 1197–1206.
129. Ghosh, A. and Lee, Y.H. (2012) *ChemSusChem*, **5**, 480–499.
130. Zhang, L., Yang, X., Zhang, F., Long, G., Zhang, T., Leng, K., Zhang, Y., Huang, Y., Ma, Y., and Zhang, M. (2013) *J. Am. Chem. Soc.*, **135**, 5921–5929.
131. Huang, J.S., Sumpter, B.G., and Meunier, V. (2008) *Chem. Eur. J.*, **14**, 6614–6626.
132. Kajdos, A., Kvit, A., Jones, F., Jagiello, J., and Yushin, G. (2010) *J. Am. Chem. Soc.*, **132**, 3252.

133. Vix-Guterl, C., Frackowiak, E., Jurewicz, K., Friebe, M., Parmentier, J., and Béguin, F. (2005) *Carbon*, **43**, 1293–1302.
134. Inagaki, M., Konno, H., and Tanaike, O. (2010) *J. Power Sources*, **195**, 7880–7903.
135. Xia, K., Gao, Q., Jiang, J., and Hu, J. (2008) *Carbon*, **46**, 1718–1726.
136. Korenblit, Y., Rose, M., Kockrick, E., Borchardt, L., Kvit, A., Kaskel, S., and Yushin, G. (2010) *ACS Nano*, **4**, 1337–1344.
137. Xing, W., Huang, C., Zhuo, S., Yuan, X., Wang, G., Hulicova-Jurcakova, D., Yan, Z., and Lu, G. (2009) *Carbon*, **47**, 1715–1722.
138. Tanahashi, I., Yoshida, A., and Nishino, A. (1990) *J. Electrochem. Soc.*, **137**, 3052–3057.
139. Wang, H.L., Gao, Q.M., and Hu, J. (2010) *Microporous Mesoporous Mater.*, **131**, 89–96.
140. Jurewicz, K., Babeł, K., Źiółkowski, A., and Wachowska, H. (2003) *Electrochim. Acta*, **48**, 1491–1498.
141. Pandolfo, A.G. and Hollenkamp, A.F. (2006) *J. Power Sources*, **157**, 11–27.
142. Radeke, K., Backhaus, K., and Swiatkowski, A. (1991) *Carbon*, **29**, 122–123.
143. Polovina, M., Babić, B., Kaluderović, B., and Dekanski, A. (1997) *Carbon*, **35**, 1047–1052.
144. Lota, G., Lota, K., and Frackowiak, E. (2007) *Electrochem. Commun.*, **9**, 1828–1832.
145. Gu, W. and Yushin, G. (2013) *Wiley Interdiscip. Rev. Energy Environ.*, **3** (5), 424–473. doi: 10.1002/wene.102
146. Avraham, E., Yaniv, B., Soffer, A., and Aurbach, D. (2008) *J. Phys. Chem. C*, **112**, 7385–7389.
147. Noked, M., Avraham, E., Bohadana, Y., Soffer, A., and Aurbach, D. (2009) *J. Phys. Chem. C*, **113**, 7316–7321.
148. Choi, N.S., Chen, Z., Freunberger, S.A., Ji, X., Sun, Y.K., Amine, K., Yushin, G., Nazar, L.F., Cho, J., and Bruce, P.G. (2012) *Angew. Chem. Int. Ed.*, **51**, 9994–10024.
149. Korenblit, Y., Kajdos, A., West, W.C., Smart, M.C., Brandon, E.J., Kvit, A., Jagiello, J., and Yushin, G. (2012) *Adv. Funct. Mater.*, **22**, 1655–1662.
150. Miller, J.R. and Simon, P. (2008) *Sci. Mag.*, **321**, 651–652.
151. Evanoff, K., Khan, J., Balandin, A.A., Magasinski, A., Ready, W.J., Fuller, T.F., and Yushin, G. (2012) *Adv. Mater.*, **24**, 533–537.
152. Yuan, L., Feng, J., Ai, X., Cao, Y., Chen, S., and Yang, H. (2006) *Electrochem. Commun.*, **8**, 610–614.
153. Brunauer, S., Emmett, P.H., and Teller, E. (1938) *J. Am. Chem. Soc.*, **60**, 309–319.
154. Ravikovitch, P.I., Vishnyakov, A., Russo, R., and Neimark, A.V. (2000) *Langmuir*, **16**, 2311–2320.
155. Lee, S.-I., Saito, K., Kanehashi, K., Hatakeyama, M., Mitani, S., Yoon, S.-H., Korai, Y., and Mochida, I. (2006) *Carbon*, **44**, 2578–2586.
156. Wang, H., Köster, T.K.-J., Trease, N.M., Ségalini, J., Taberna, P.-L., Simon, P., Gogotsi, Y., and Grey, C.P. (2011) *J. Am. Chem. Soc.*, **133**, 19270–19273.
157. Borchardt, L., Oschatz, M., Paasch, S., Kaskel, S., and Brunner, E. (2013) *Phys. Chem. Chem. Phys.*, **15**, 15177–15184.
158. Deschamps, M., Gilbert, E., Azais, P., Raymundo-Piñero, E., Ammar, M.R., Simon, P., Massiot, D., and Béguin, F. (2013) *Nat. Mater.*, **12**, 351–358.
159. Boukhalfa, S., He, L., Melnichenko, Y.B., and Yushin, G. (2013) *Angew. Chem. Int. Ed.*, **52**, 4618–4622.
160. Randin, J.-P. and Yeager, E. (1970) Differential Capacitance Study of Stress-Annealed Pyrolytic Graphite Electrodes, DTIC Document.
161. Randin, J.-P. and Yeager, E. (1972) *J. Electroanal. Chem. Interfacial Electrochem.*, **36**, 257–276.
162. Randin, J.-P. and Yeager, E. (1975) *J. Electroanal. Chem. Interfacial Electrochem.*, **58**, 313–322.
163. Gerischer, H., McIntyre, R., Scherson, D., and Storck, W. (1987) *J. Phys. Chem.*, **91**, 1930–1935.
164. Gerischer, H. (1985) *J. Phys. Chem.*, **89**, 4249–4251.
165. Dröscher, S., Roulleau, P., Molitor, F., Studerus, P., Stampfer, C., Ensslin, K., and Ihn, T. (2010) *Appl. Phys. Lett.*, **96**, 152104.

166. Xia, J., Chen, F., Li, J., and Tao, N. (2009) *Nat. Nanotechnol.*, **4**, 505–509.

167. Ponomarenko, L., Yang, R., Gorbachev, R., Blake, P., Mayorov, A., Novoselov, K., Katsnelson, M., and Geim, A. (2010) *Phys. Rev. Lett.*, **105**, 136801.

168. Jang, I.Y., Muramatsu, H., Park, K.C., Kim, Y.J., and Endo, M. (2009) *Electrochem. Commun.*, **11**, 719–723.

169. Zhang, L.L., Zhao, X., Ji, H., Stoller, M.D., Lai, L., Murali, S., Mcdonnell, S., Cleveger, B., Wallace, R.M., and Ruoff, R.S. (2012) *Energy Environ. Sci.*, **5**, 9618–9625.

170. Korai, Y., Qiao, W., Mochida, I., Hori, Y., and Maeda, T. (2002) *Carbon*, **40** (3), 351–358.

171. Nishihara, H., Itoi, H., Kogure, T., Hou, P.X., Touhara, H., Okino, F., and Kyotani, T. (2009) *Chem. Eur. J.*, **15**, 5355–5363.

172. Pell, W.G., Conway, B.E., and Liu, T.-C. (1997) *J. Power Sources*, **65** (1–2), 53–59.

173. Pell, W.G., Liu, T.-C., and Conway, B.E. (1996) *Electrochim. Acta*, **42** (23-24), 3541–3552.

174. Kaus, M., Kowal, J., and Sauer, D.U. (2010) *Electrochim. Acta*, **55**, 7516–7523.

175. Venet, P., Diab, Y., Gualous, H., and Rojat, G. (2009) *IEEE Trans. Power Electron.*, **24** (2), 510–517.

176. Zhang, X., Wang, X., Su, J., Wang, X., Jiang, L., Wu, H., and Wu, C. (2012) *J. Power Sources*, **199**, 402–408.